Geophysical Research Letters

RESEARCH LETTER
10.1029/2025GL116809

Structure Heterogeneity Around the Western End of the 1999 Izmit Earthquake Rupture Revealed by Distributed Acoustic Sensing

Ji Zhang[1], Aitaro Kato[1], Wei Wang[2,3], Shigeki Nakagawa[1], and Ahmet Anil Dindar[4]

[1]Earthquake Research Institute, The University of Tokyo, Tokyo, Japan, [2]Key Laboratory of Planetary Science and Frontier Technology, Institute of Geology and Geophysics, Chinese Academy of Sciences, Beijing, China, [3]College of Earth and Planetary Sciences, University of Chinese Academy of Sciences, Beijing, China, [4]MARTEST Research and Training Center, Gebze Technical University, Kocaeli, Türkiye

Key Points:

- 2D shear-wave velocity structure from submarine distributed acoustic sensing using ambient noise method across the North Anatolian Fault
- Fault distribution imaged by autocorrelation method and natural migration
- Wide fracture zone and geometric complexity may act as a soft barrier that controls rupture dynamics and stress accumulation

Supporting Information:

Supporting Information may be found in the online version of this article.

Correspondence to:

A. Kato,
akato@eri.u-tokyo.ac.jp

Citation:

Zhang, J., Kato, A., Wang, W., Nakagawa, S., & Dindar, A. A. (2025). Structure heterogeneity around the western end of the 1999 Izmit earthquake rupture revealed by distributed acoustic sensing. *Geophysical Research Letters*, *52*, e2025GL116809. https://doi.org/10.1029/2025GL116809

Received 6 MAY 2025
Accepted 29 SEP 2025

Author Contributions:

Conceptualization: Ji Zhang, Aitaro Kato, Wei Wang, Shigeki Nakagawa, Ahmet Anil Dindar
Data curation: Ji Zhang
Funding acquisition: Aitaro Kato
Investigation: Aitaro Kato
Methodology: Ji Zhang, Aitaro Kato
Project administration: Aitaro Kato, Ahmet Anil Dindar
Resources: Ji Zhang
Supervision: Aitaro Kato, Wei Wang, Shigeki Nakagawa, Ahmet Anil Dindar
Writing – original draft: Ji Zhang
Writing – review & editing: Ji Zhang, Aitaro Kato, Wei Wang, Shigeki Nakagawa, Ahmet Anil Dindar

Abstract We use distributed acoustic sensing along a submarine fiber-optic cable to provide the first high-resolution two-dimensional shear-wave velocity (Vs) model of the North Anatolian Fault (NAF) in the Marmara Sea. Using 7 days of ambient noise recordings, we extract Scholte wave dispersion curves via slant-stacking and invert for the Vs structure, identifying a pronounced low-velocity layer (~0.6 km/s), indicative of unconsolidated sediments. Autocorrelation and natural migration profiles reveal a ~3-km-wide fracture zone (WFZ), which we interpret as a legacy of long-term slip on the NAF. The low Vs and structural complexity suggest the WFZ functions as a soft barrier. Hence, it could have contributed to arrest rupture propagation during the 1999 M7.6 Izmit earthquake, as well as partitioning stress between fault segments. We also resolve a flower-like structure of faults. These results may demonstrate how fault zone heterogeneity controls rupture dynamics and stress accumulation, offering mechanistic insights into seismic segmentation.

Plain Language Summary Distributed acoustic sensing (DAS) is a state-of-the-art measurement method that has the potential to convert existing fiber-optic communication infrastructure into arrays of thousands of seismic sensors. In this study, we connected a DAS system to a fiber-optic cable that was originally installed on the seafloor to sustain a seismic observatory in the Marmara Sea. Leveraging this new type of measurement, we can provide reliable information with which to image and explore the shallow subsurface under the cable. We can use ambient noise analysis and other methodologies to image the shear-wave velocity structure and fault systems. Our results contribute to estimating the state of submarine faults, which has significant implications for disaster prevention and mitigation.

1. Introduction

The North Anatolian Fault (NAF) is a dextral continental transform boundary fault (Gasperini et al., 2021; Şengör et al., 2005) with a slip rate of 20–30 mm/yr (Reilinger et al., 2006). The segment of the NAF in the Marmara Sea represents a seismic gap capable of generating an $M \geq 7.2$ earthquake (Bohnhoff et al., 2013), directly endangering the 15 million people residing in the province of Istanbul. Despite extensive studies of the onshore NAF (e.g., Kurt et al., 2013; Lange et al., 2019), critical gaps remain in our understanding of the offshore fault geometry and locking state as a result of observational challenges (e.g., Becker et al., 2023; Yılmaz et al., 2022). Here we present the first application of distributed acoustic sensing (DAS) along a submarine telecommunication cable crossing the northern strand of the NAF in Marmara Sea, providing new constraints on fault zone structure and segmentation at an unprecedented resolution.

DAS has emerged as a transformative technology for seismic monitoring (Hartog, 2018), with applications ranging from urban seismology (Zhu & Stensrud, 2019) to the imaging of submarine faults (Cheng et al., 2021; Fukushima et al., 2022; Lindsey et al., 2019; Spica et al., 2020, 2022). Our work targets the complicated and seismically active transition zone between the locked Princes' Islands (PI) and Izmit-Düzce (ID) segments of the NAF (Figures 1 and 4), a critical boundary that may control future rupture propagation. The PI fault segment represents a dangerous seismic gap, with geodetic data indicating significant strain accumulation (e.g., Ergintav et al., 2014; Hubert-Ferrari et al., 2000) since the last major earthquakes in 1999 (Mw 7.4 Izmit and Mw 7.1 Düzce events).

10.1029/2025GL116809

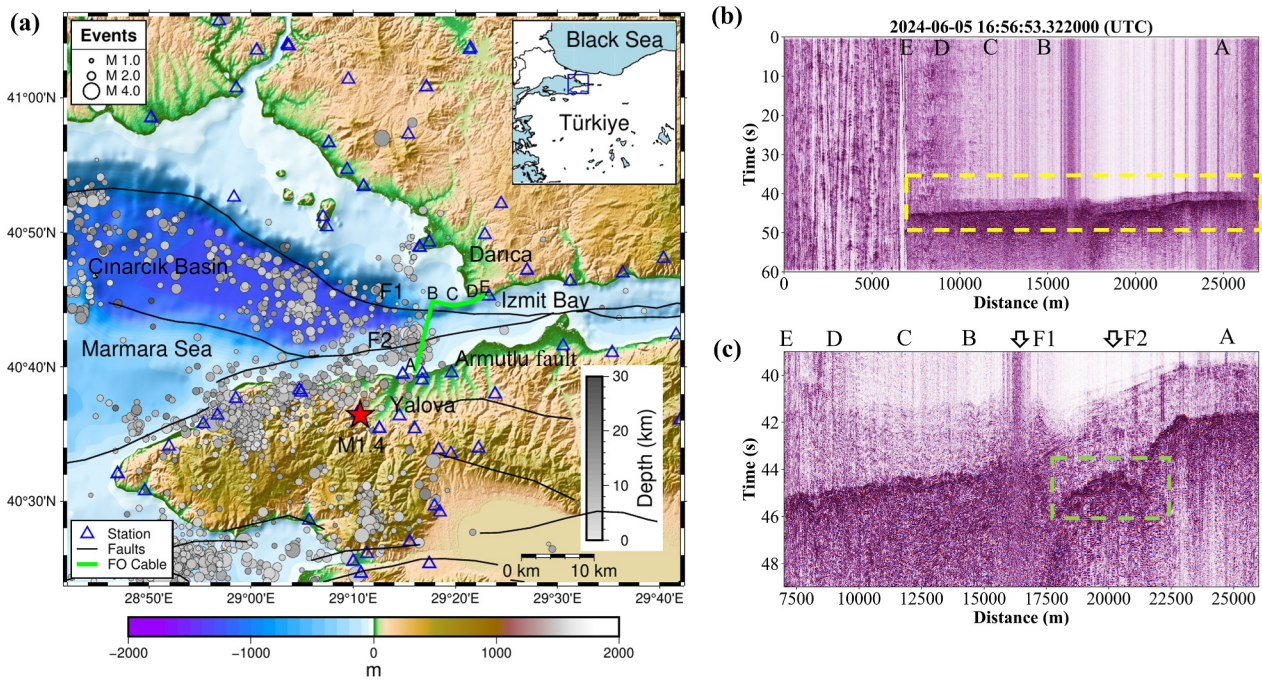

Figure 1. *Location of the study region and an example distributed acoustic sensing (DAS) record.* (a) Topographic map showing the location of the telecommunication fiber-optic cable across Izmit Bay. The fiber-optic cable (green line) used in our analysis spans ∼18 km of the seafloor. The black lines indicate surface fault traces of the North Anatolian Fault. The cable crosses the F1 and F2 faults. The colored circles represent seismic events that occurred between 1 January 2019 and 1 December 2024, and were recorded by regional seismic stations (blue triangles). The red star depicts the location of an earthquake (5 June 2024 16:57:29, $M = 1.4$) that was recorded by the DAS system. (b) DAS data for the M1.4 event, with an epicenter at 16.2 km depth (red star in panel (a)). (c) Enlargement of the area indicated by the dashed yellow rectangle in panel (b), showing the first arrivals. A hyperbolic shape is visible around 21 km along the fiber-optic cable, as highlighted by the dashed green rectangle.

We use DAS to transform the 27 km of fiber-optic cable spanning the submarine fault segments into 8,275 seismic sensors (3.26-m spacing) to extract the high-resolution shear-wave velocity (Vs) structure and fault architecture, thereby overcoming the spatial limitations of conventional ocean-bottom seismometers (Sladen et al., 2019; Zhan, 2019). By combining ambient noise tomography, autocorrelation profiling, and natural migration imaging, we delineate a ∼3-km-wide fracture zone (WFZ) and a complex flower-like structure of faults along the fault boundary that may serve as a rupture barrier (e.g., Kato et al., 2010). Our findings provide new constraints on fault segmentation, stress accumulation, and potential rupture barriers along the NAF, with implications for seismic hazard assessment in the Marmara region. These results provide critical insights into the influence of structural

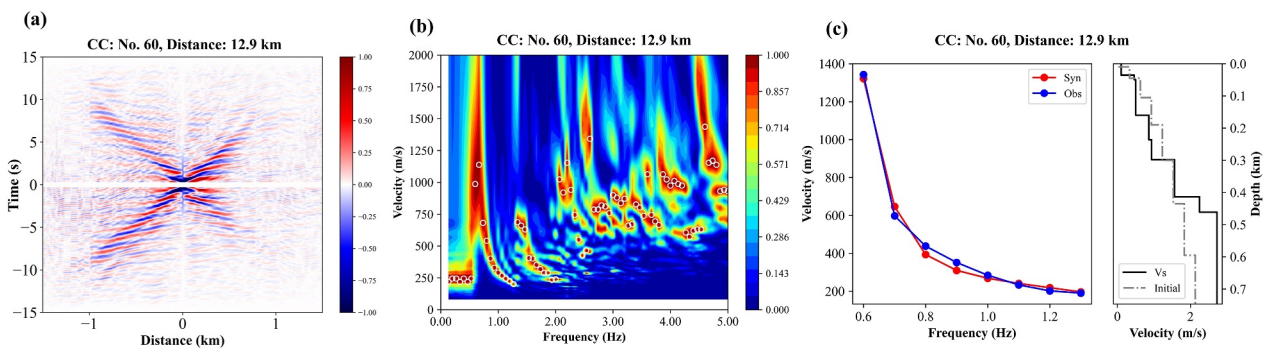

Figure 2. *Ambient noise tomography.* (a) Empirical Green's function extracted from the virtual source records using the ambient noise method. Colorbar shows normalized amplitude. (b) Scholte wave dispersion curve obtained from cross-correlations using the slant-stacking method. The white circles indicate the phase velocity corresponding to each frequency. Colorbar shows normalized energy. (c) Phase velocity and Vs structures inverted from dispersion curves using the simulated annealing algorithm. The blue and red lines indicate the observed and synthetic dispersion curves, respectively. The black and gray lines indicate the Vs structure and the initial velocity model, respectively.

complexity on rupture dynamics along faults, while also establishing a new paradigm for seismic hazard assessment in submarine environments.

2. Data

We use a communication fiber-optic cable that extends across Izmit Bay in the Marmara Sea, from Darıca in the north to Yalova in the south of Izmit Bay, as shown in Figure 1a. The cable is deployed partially on land and partially along the seafloor, with the submarine segment crossing two active transpressive faults and continuing along a submarine trench. Due to limited accessibility, the detailed location of the seafloor cable is unavailable, as Turk Telecom has provided only five location points for the cable. Although only these five positions are known with confidence, the cable appears to follow a nearly linear path between them, allowing interpolation of the intermediate segment positions. Based on this configuration, we estimate the spatial uncertainty to be modest (on order of ∼100 m), with minimal impact on the interpretation of large-scale features. The submarine segment of the fiber optic cable, which spans points A to E in Figure 1a, extends along 18 km of the seafloor. Analysis of coda waves from regional events suggests that the submarine cable coupling is relatively uniform along the array. Furthermore, the precise location of the on-land portion of the cable is unknown. Therefore, this study focuses on the submarine DAS data.

We started the DAS measurements along the communication fiber-optic cable on 26 May 2024 and acquired continuous data for ∼7 days in the Marmara Sea. The DAS interrogator unit (Nippon Electric Company, Japan) was installed in Darıca, and strain rate data were recorded along the entire 27-km length at a spatial resolution of 3.26 m and sampling frequency of 1,000 Hz. There were 8,275 channels along the cable, and the gauge length was set to 6.4 m. Note that the gauge length refers to the spatial resolution of the fiber-optic sensor, which is essentially the measurement interval or sampling distance along the fiber-optic cable, representing the cable length over which each measurement is averaged. Here we focus on the 18-km-long submarine segment of the cable, which extends from 7 to 25 km along the cable.

3. Methods

3.1. Ambient Noise Tomography

We apply ambient noise interferometry techniques (Weaver, 2005) to extract the coherent signals from the DAS records. The raw DAS data are somewhat not directly suitable for ambient noise imaging, thereby requiring pre-processing, filtering at 0.01–10 Hz, and downsampling (from 1,000 to 100 Hz) prior to analysis. Our analysis follows the established workflow for ambient noise data processing (Bensen et al., 2007) to obtain the empirical Green's functions for the 7-day continuous DAS data set by processing 60-s data segments. The dense spatial sampling of the DAS array and the relatively stable conditions of the seafloor enable the extraction of reliable surface wave signals, even from short-duration recordings. Previous studies have demonstrated the feasibility of velocity model inversion using limited DAS data—for example, Spica et al. (2022) used approximately 46 hr of offshore DAS recordings along the Sanriku cable, and Cheng et al. (2021) used 4 days of data from the MARS cable. In our data set, stable and coherent virtual sources are clearly observed using 7 days of recording (Figure S1 in Supporting Information S1), confirming that the data set is of sufficient quality to support robust surface wave dispersion analysis and velocity inversion. The raw DAS data are first demeaned and detrended, with time domain normalization using the running absolute mean filter and spectral whitening processing then applied. We select the channels from 7 to 25 km along the cable as virtual sources, with the source spatial interval set at 98 m to obtain 185 virtual sources. We generate the cross-correlation (CC) results between each virtual source and 938 channels within 3 km (from −1.5 to +1.5 km offset) of each source (Figure 2a). We do not use all the channels because those that are too far from the virtual source are highly uncorrelated (Figure S1 in Supporting Information S1).

We apply a frequency domain slant-stacking algorithm (Park et al., 1998; Sacchi & Ulrych, 1995) to each virtual gather to obtain the Scholte wave dispersion spectra (Williams et al., 2021) (Figure 2b). To extract surface wave dispersion curves, we employ a slant-stacking technique that aligns seismic traces using a range of trial slowness values, thereby amplifying coherent wave energy through stacking. The resulting frequency–slowness maps are used to estimate phase velocities across the observed frequency band. We enhanced the extraction of the dispersion curve by applying a mask to the CC results (Figure S2 in Supporting Information S1). The mask range was determined from the correlation of the dispersion curve, effectively mitigating the influence of low-velocity

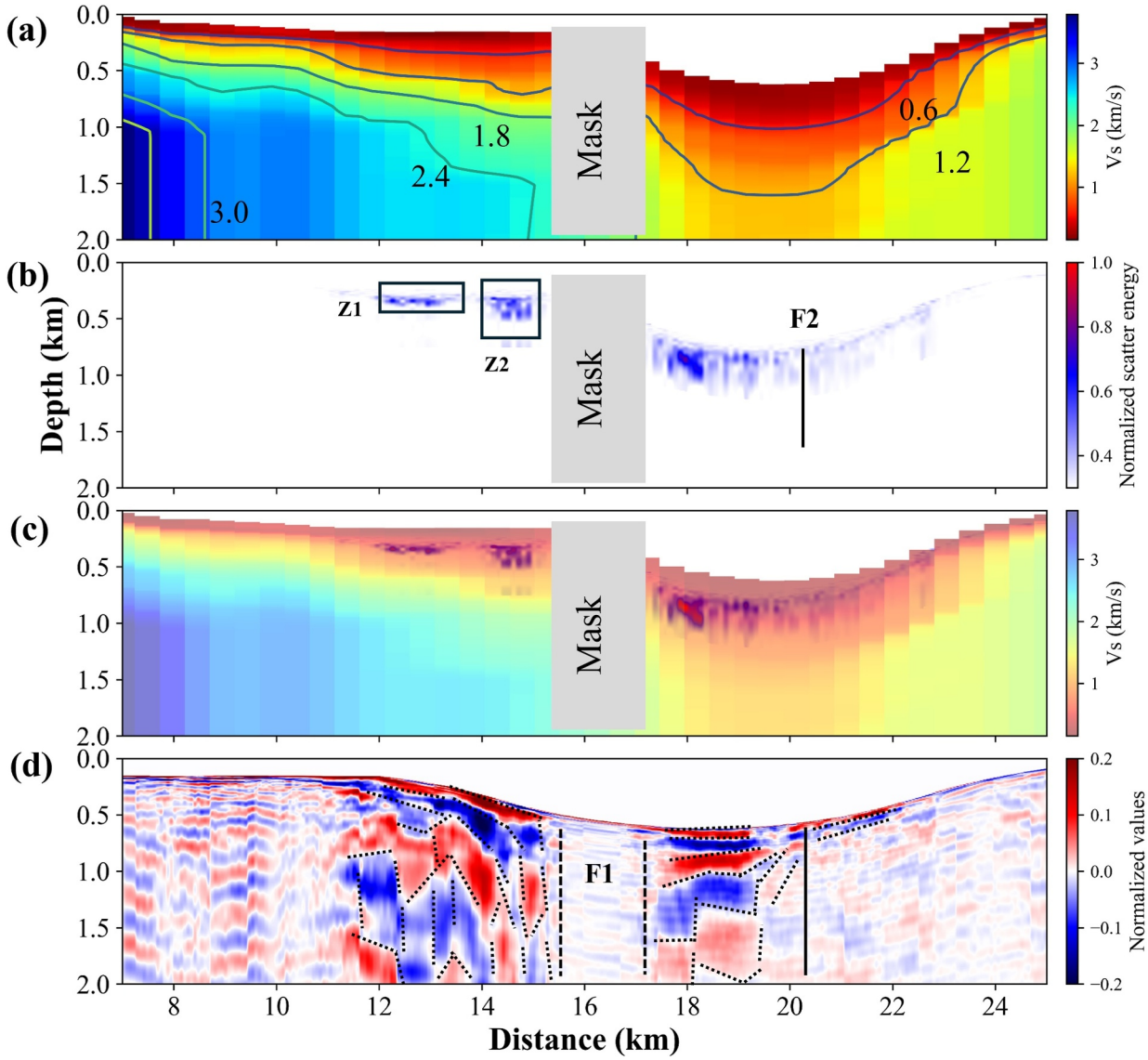

Figure 3. *Submarine structures*. (a) 2D Vs structures. (b) Scholte wave scattering location using the natural migration method. Zones Z1 and Z2 have strong scattered energy. Solid line indicates the F2 fault location. (c) Combined Vs structure and migration results. (d) Autocorrelation profile from near-offset channels in the virtual source gathers. Dotted lines show the flower-like structure of faults. Dashed lines show the masked noisy region around the F1 fault.

components. To ensure high data quality and avoid misidentification, we manually picked only well-defined ridges of energy corresponding to the fundamental mode from frequency–velocity spectra. Although higher-order modes were observed in some segments, they lacked sufficient coherence to be used reliably. We employed simulated annealing (SA, Text S1 in Supporting Information S1) algorithm (Kirkpatrick, 1984) to invert for Vs and the layer thickness (Herrmann, 2013). The initial model (Figure 2c) was defined as a smooth ten-layer profile based on typical shallow marine sediment velocities and regional geological constraints (Polat et al., 2016). During inversion, Vs values were bounded between 0.1 and 3.0 km/s, with individual layer thickness ranging from 10 to 500 m. An example of the observed and synthetic dispersion curves, along with the corresponding inverted Vs, is shown in Figure 2c. The ability of the SA method to balance exploration and exploitation makes it well-suited for phase-velocity curve inversion. We can obtain the Vs structure from each virtual source (Figure S3 in Supporting Information S1) and then integrate them to obtain the 2D Vs structure, as shown in Figure 3a.

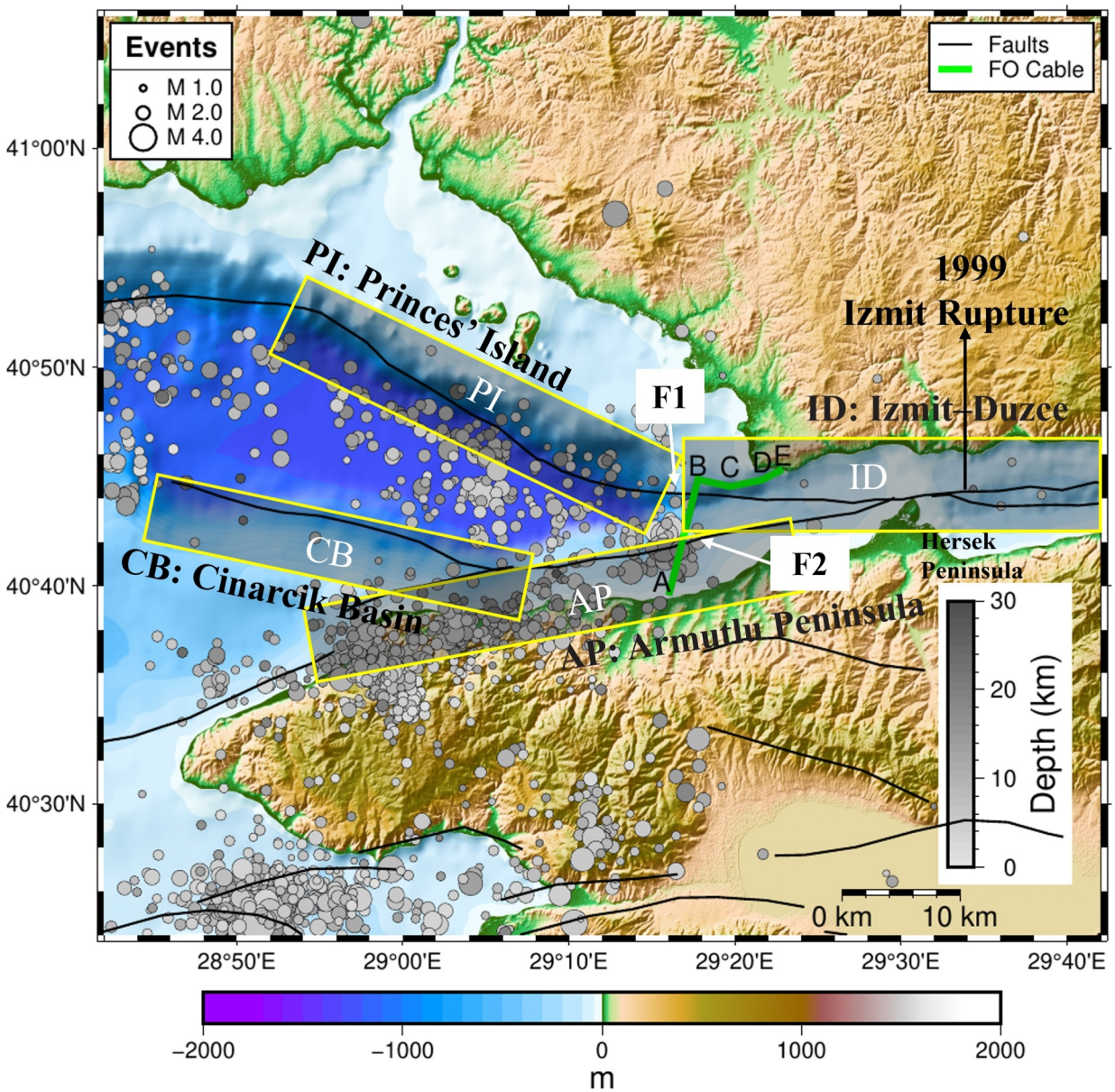

Figure 4. *North Anatolian Fault Zone in northwestern Türkiye*. Distribution of fault systems, specifically Princes' Islands, Cinarcik Basin, Izmit-Düzce (ID), and Armutlu Peninsula, with the ID fault representing the rupture from the 1999 Izmit earthquake. The boxes represent the extent of fault zones. The earthquake data are the same as in Figure 1a.

3.2. Natural Migration of Scattered Scholte Waves

Backscattered surface waves can be used to image near-surface heterogeneities through natural migration, which leverages the recorded Green's functions along the surface (Liu et al., 2017). While natural migration images (Altheyab et al., 2016) were originally developed for free-surface environments, the seabed represents a water–solid boundary with distinct wavefield characteristics. Nevertheless, surface waves in such environments still retain frequency-dependent depth sensitivity, enabling the investigation of subsurface structures (Cheng et al., 2021). This property makes natural migration a powerful tool for characterizing near-seafloor features in submarine environments. The migration equation for the DAS-observed backscattered surface wave is

$$m(\boldsymbol{x},\omega 0) = \iiint \beta_{\omega 0}(\omega)\, \overline{G(\boldsymbol{x}|\boldsymbol{x}_s)\, G^0(\boldsymbol{x}|\boldsymbol{x}_r)}\, u(\boldsymbol{x}_s,\boldsymbol{x}_r)\, d\boldsymbol{x}_s\, d\boldsymbol{x}_r\, d\omega,$$

where $\beta_{\omega 0}(\omega)$ is the bandpass filter designed to smoothly taper the data and Green's tensors around the central frequency $\omega 0$; $G(\boldsymbol{x}|\boldsymbol{x}_s)$ is the empirical Green's function obtained by cross-correlating ambient noise records, with a virtual source at location x_s and receiver at location x; $G^0(\boldsymbol{x}|\boldsymbol{x}_r)$ is the empirical Green's function retrieved with a virtual source at location x_r and receiver at location x, containing only the transmitted wavefield without back-scattering; $u(\boldsymbol{x}_s, \boldsymbol{x}_r)$ is the separated scattered wavefield; and $m(\boldsymbol{x}, \omega 0)$ is the scatter image energy at location x and frequency $\omega 0$. The wavefield separation is performed using a frequency–wavenumber (FK) filter, a method commonly used for up/down wavefield separation. For natural migration, we utilize 185 virtual source gathers along the cable, with each gather consisting of 625 channels. Natural migration is conducted in the frequency domain to improve computational efficiency, thereby replacing the bandpass filter with a median filter applied to the output natural migration spectrum. Finally, the frequency-dependent scattering image is converted to depth or wavelength using an average dispersion curve derived from an averaged velocity model (500 m/s) beneath the cable. The resultant natural migration image is shown in Figure 3b. The consistency between natural migration images, cross-correlation results, and prior structural studies (Beyhan et al., 2009; Gasperini et al., 2021; Kurt et al., 2013) indicates that the observed scattering features are both robust and geologically meaningful. We also integrate the 2D Vs structure from the ambient noise tomography and natural migration imaging to characterize the submarine structure, as shown in Figure 3c.

3.3. Autocorrelation Profile

Autocorrelations (ACs) derived from stacks of the near-offset channels in virtual source gathers are used to create an image of the deeper subsurface. This approach produces a zero-offset reflection image of the subsurface using ambient noise correlation. This technique is particularly effective for imaging the lateral discontinuity of subsurface layers (Clayton, 2020). While AC peaks can be influenced by site response effects, such as variations in dominant frequency, the agreement between the AC image, CC-derived velocity variations, and natural migration results supports the interpretation that these features predominantly reflect true subsurface structures. The AC (zero-offset) profile at point x is approximated by stacking cross-correlation pairs with small offsets (less than 600 m) and positioning midpoints of the pairs along the DAS array, as shown in Figure S4a in Supporting Information S1. To better constrain the location of subsurface structures, we performed a time–depth conversion using the inverted velocity model. This conversion facilitates a clearer interpretation of the depth extent of the fault zone features identified in the AC image (Figure 3d). The resultant AC profile indicates a distinct lateral variation along the submarine cable at a high spatial resolution, achieved by computing one AC result every 32 m. To enhance our understanding of scattered Scholte wave components, we apply a running window FK filter (100 m/s $< v <$ 1,000 m/s) along the profile to amplify these weak scattered arrivals, as shown in Figure S4b in Supporting Information S1. Our observations indicate that most of these scattered arrivals originate at lateral discontinuity boundaries, particularly at 17 and 20 km along the DAS profile.

Our multimethod imaging strategy integrates ambient noise tomography, AC imaging, and natural migration, each offering complementary strengths in spatial sampling, depth sensitivity, and structural resolution. Ambient noise tomography yields 1D shear-wave velocity profiles at 500 m intervals along the array, with depth sensitivity spanning from approximately 200 to 1,000 m, effectively constraining the upper crustal velocity structure. Autocorrelation imaging, performed every 32 m using 600 m data windows, enhances the detection of lateral discontinuities and sharp impedance contrasts, although it lacks absolute velocity information. Natural migration, like AC, targets structural boundaries but additionally incorporates velocity information extracted from background noise, enabling improved depth localization of subsurface reflectors. In combination, these complementary methods provide a synergistic framework for more effectively interpreting fault zone heterogeneity.

4. Discussion

Our DAS observations reveal a distinct hyperbolic feature at ~21 km along the DAS profile (Figure 1c), which we interpret as evidence for the southern branch of the NAF, referred to here as F2 fault (Figure 1a). This geometry is consistent with seismic wave scattering at fault interfaces (e.g., Beyhan et al., 2009). While the hyperbolic *S*-wave travel-time feature aligns with the location of the F2 fault (Figure 1c) and may indicate a deeper structural contrast, this interpretation remains tentative due to the limited resolution of the shallow velocity model (~0.5 km depth). A more rigorous assessment would require refining the shallow velocity structure by correcting *S*-wave

travel times, and analyzing the residuals to isolate signals associated with deeper fault-zone features. These improvements will be pursued in future work.

The 2D Vs structure along the cable reveals low velocities in the shallow layers (~0.6 km/s, Figure 3a), which are characteristic of high-porosity marine sediments (Hamilton, 1979). The inverted Vs structure aligns with the observed sensitivity depths (~0.5 km, Figure S5 in Supporting Information S1), thereby confirming the reliability of our velocity model. Both AC and natural migration produce time-domain images, converted to depth using a velocity model. Their depth sensitivity thus depends on the model. We approximate it by summing depth sensitivity kernels from the inverted model and multiplying them with the depth-domain AC and natural migration (Figures S5c and S5d in Supporting Information S1). Of note, integrating the 2D pervasive scattering energy and low-velocity trench structures (Figure 3b) suggests the presence of a ~3-km-wide WFZ that consists of two major faults (F1 and F2) and unrecognized minor faults that likely formed during the long-term movement of the NAF. However, data limitations near F1 prevent a fully constrained spatial characterization. Zones Z1 and Z2 may correspond to offshore fractures and topographic transitions, respectively, with the latter potentially influencing cable coupling. The relatively weak scattered energy suggests natural migration faults are largely confined to the shallow layers, although deeper extensions cannot be ruled out, given the low energy levels in the data.

The AC profile (Figure 3d) highlights lateral discontinuities, with F2 being apparent and masking being applied to noisy regions. The noisy data near F1 (Figure S4c and S4d in Supporting Information S1) complicate the velocity inversion and migration (Figures 3a–3c). Moreover, spectral analysis (Figure S6 in Supporting Information S1) reveals low-frequency signals that are challenging to detect in this zone, potentially indicating the influence of F1 (Figure 3d). The AC profile, combined with ambient noise data (Figure S4c in Supporting Information S1) and DAS records of the M3.8 event (26 May 2024, 21:38:18; Figure S4d in Supporting Information S1) located ~82 km from the cable, reveals terrain transitions, thereby refining geological interpretations. Integrating natural migration results with the AC profile shows lateral discontinuities, suggesting the presence of a complex flower-like structure of faults. Similar flower structures have been identified along the NAF in the Marmara Sea (Beyhan et al., 2009; Gasperini et al., 2021; Kurt et al., 2013), thereby supporting our results. Figure 3c indicates that numerous small fractures are concentrated within the trench (17–21 km along the profile), likely forming the core of the flower structure.

The fiber-optic cable runs along the western boundary of the rupture zone of the 1999 M7.6 Izmit earthquake (Bohnhoff et al., 2013), near the fault segment boundary between the ID region and the PI region in the Cinarcik Basin (Figure 4). Multiple independent observations support the hypothesis that the 1999 Izmit earthquake rupture terminated near this ID–PI boundary. The aftershock distribution shows a significant reduction in seismicity west of the ID–PI boundary (Bohnhoff et al., 2006), consistent with rupture arrest in that region. Wright et al. (2001) located the rupture's western limit approximately 15 km west of the Hersek Peninsula (~29.3°E), based on InSAR-derived slip models. Similarly, morphological evidence from subaqueous escarpment videos also indicates an abrupt change in fault expression near this location (Armijo et al., 2005). More recently, Amemoutou et al. (2023) also identified rupture termination near this boundary. While direct confirmation is hindered by the submarine setting, in combination, these data sets indicate that the rupture likely stopped or significantly slowed down near the ID–PI boundary.

To the west of the cable, recent seismic activity has been relatively high compared with that along the ID fault segment (Figure 4). This reduction in seismicity is likely a consequence of substantial shear stress release during the 1999 Izmit rupture, similar to shutdown of on-fault seismicity observed following other major earthquakes, such as the 2011 M9.0 Tohoku-Oki event (e.g., Kato & Igarashi, 2012). Thus, the WFZ, characterized by a low seismic velocity structure and small-scale fracturing, may act as a soft barrier that impedes the dynamic rupture propagation from the ID segment. However, this barrier may not always be sufficient to halt rupture propagation entirely (Wang et al., 2024). Although analogous features have been associated with rupture arrest in shallow subduction zones, the distinct tectonic setting and rupture behavior of the Izmit earthquake make such comparisons nontrivial. Therefore, we consider the soft barrier interpretation as plausible but not definitive. The WFZ may serve to limit the transfer of seismic energy from the ID segment to the adjacent PI or Armutlu Peninsula (AP) segments. Along the PI fault segment, seafloor measurements of relative fault displacement suggest complete fault locking to a depth of at least 10 km (Lange et al., 2019). Furthermore, the rupture of the 1999 Izmit

earthquake has increased stress along the PI and AP segments (Amemoutou et al., 2023), indicating stress loading from the Izmit earthquake onto these locked sections adjacent to the rupture terminus.

The geometrical complexity may have also contributed to the termination of the Izmit earthquake rupture (Ben-Zion & Sammis, 2003), because the fault strike and dip direction differ between the ID segment and the adjacent PI and AP segments. Numerical modeling by Aochi and Madariaga (2003) further has demonstrated that fault geometry and prestress play a critical role in the Izmit earthquake rupture propagation. An alternative explanation is that the rupture might be arrested at approximately 15 km west of the Hersek Peninsula due to a stress shadow left by the 1894 ($M \sim 7$) earthquake (Harris et al., 2002). Taken together, these findings suggest that the observed rupture termination likely reflects the combined effects of stress heterogeneity and structural/rheological complexity. Future dynamic rupture modeling incorporating these constraints could further test the relative importance of each factor. In addition, further research is needed to resolve the lateral changes in fine velocity structure along the NAF.

DAS provides a cost-effective approach to submarine fault monitoring, requiring only interrogator units and existing fiber-optic cables. Applied to subduction zones (e.g., the Nankai Trough, Japan) and/or transform faults (e.g., the San Andreas Fault, California, USA), DAS could enable high-resolution imaging of submarine fault segments at a lower cost than traditional ocean-bottom seismometer arrays. This scalability positions DAS as a key technology for next-generation seismic hazard assessment in subduction and transform fault systems.

5. Conclusions

Our seafloor DAS observations provide new high-resolution evidence of the potential role of fault zone heterogeneity in influencing seismic segmentation along the NAF in the Marmara Sea. The wide fracture zone, with its low-velocity sediments and geometric complexity, may act as a soft barrier, partitioning stress between the creeping (PI segment) and locked (ID segment) regions of the fault system. This heterogeneity explains the termination of the 1999 Izmit rupture and highlights the seismic gap offshore from Istanbul. By transforming submarine cables into tectonic sensors, DAS provides a scalable framework with which to monitor fault states globally, particularly in understudied submarine seismic gaps (e.g., Nankai Trough). Real-time integration with geodetic data could revolutionize probabilistic hazard assessment for megacities such as Istanbul.

Conflict of Interest

The authors declare no conflicts of interest relevant to this study.

Data Availability Statement

The event catalog was provided by the Kandilli Observatory and Earthquake Research Institute (KOERI: http://www.koeri.boun.edu.tr/sismo/2/earthquake-catalog/). The cross-correlation data (Zhang, 2025a, https://doi.org/10.5281/zenodo.16741982) and the event waveform data (Zhang, 2025b, https://doi.org/10.5281/zenodo.15791919) used to reproduce the figures are available from the MARTEST Repository (https://zenodo.org/communities/satreps-martest/). The surface wave dispersion was computed using disba (https://github.com/keurfonluu/disba) (Luu, 2021).

Acknowledgments

The authors sincerely thank the associate editor and the two reviewers for their valuable feedback and suggestions, which have greatly improved this work. This research was supported by the Japan Society for the Promotion of Science (JSPS KAKENHI 21H05205) and SATREPS under the "Establishment of a Research and Education Complex for Developing Disaster-resilient Societies—MARTEST" project, promoted by the Japan International Cooperation Agency (JICA) and Japan Science and Technology Agency (JST).

References

Altheyab, A., Lin, F.-C., & Schuster, G. T. (2016). Imaging near-surface heterogeneities by natural migration of backscattered surface waves. *Geophysical Journal International*, *204*(2), 1332–1341. https://doi.org/10.1093/gji/ggv511

Amemoutou, A., Martínez-Garzón, P., Durand, V., Kwiatek, G., Bohnhoff, M., & Dresen, G. (2023). Spatio-temporal variations of seismic coupling along a transform fault: The western North Anatolian fault zone. *Geophysical Journal International*, *235*(2), 1982–1995. https://doi.org/10.1093/gji/ggad341

Aochi, H., & Madariaga, R. (2003). The 1999 Izmit, Turkey, earthquake: Nonplanar fault structure, dynamic rupture process, and strong ground motion. *Bulletin of the Seismological Society of America*, *93*(3), 1249–1266. https://doi.org/10.1785/0120020167

Armijo, R., Pondard, N., Meyer, B., Uçarkus, G., de Lépinay, B. M., Malavieille, J., et al. (2005). Submarine fault scarps in the Sea of Marmara pull-apart (North Anatolian fault): Implications for seismic hazard in Istanbul. *Geochemistry, Geophysics, Geosystems*, *6*(6), Q06009. https://doi.org/10.1029/2004gc000896

Becker, D., Martínez-Garzón, P., Wollin, C., Kılıç, T., & Bohnhoff, M. (2023). Variation of fault creep along the overdue Istanbul-Marmara seismic gap in NW Türkiye. *Geophysical Research Letters*, *50*(6), e2022GL101471. https://doi.org/10.1029/2022gl101471

Bensen, G. D., Ritzwoller, M. H., Barmin, M. P., Levshin, A. L., Lin, F., Moschetti, M. P., et al. (2007). Processing seismic ambient noise data to obtain reliable broad-band surface wave dispersion measurements. *Geophysical Journal International*, *169*(3), 1239–1260. https://doi.org/10.1111/j.1365-246x.2007.03374.x

Ben-Zion, Y., & Sammis, C. G. (2003). Characterization of fault zones. *Pure and Applied Geophysics*, *160*(3), 677–715. https://doi.org/10.1007/pl00012554

Beyhan, G., Selim, H. H., & Özçiçek, B. (2009). Tectonics related to the North Anatolian fault in the Sea of Marmara: Evidence from seismic reflection data. *Marine Geophysical Researches*, *30*(4), 237–250. https://doi.org/10.1007/s11001-010-9083-z

Bohnhoff, M., Bulut, F., Dresen, G., Malin, P. E., Eken, T., & Aktar, M. (2013). An earthquake gap south of Istanbul. *Nature Communications*, *4*(1), 1999. https://doi.org/10.1038/ncomms2999

Bohnhoff, M., Grosser, H., & Dresen, G. (2006). Strain partitioning and stress rotation at the North Anatolian fault zone from aftershock focal mechanisms of the 1999 Izmit Mw = 7.4 earthquake. *Geophysical Journal International*, *166*(1), 373–385. https://doi.org/10.1111/j.1365-246x.2006.03027.x

Cheng, F., Chi, B., Lindsey, N. J., Dawe, T. C., & Ajo-Franklin, J. B. (2021). Utilizing distributed acoustic sensing and ocean bottom fiber optic cables for submarine structural characterization. *Scientific Reports*, *11*(1), 5613. https://doi.org/10.1038/s41598-021-84845-y

Clayton, R. W. (2020). Imaging the subsurface with ambient noise autocorrelations. *Seismological Research Letters*, *91*(2A), 930–935. https://doi.org/10.1785/0220190272

Ergintav, S., Reilinger, R. E., Çakmak, R., Floyd, M., Cakir, Z., Doğan, U., et al. (2014). Istanbul's earthquake hot spots: Geodetic constraints on strain accumulation along faults in the Marmara seismic gap. *Geophysical Research Letters*, *41*(16), 5783–5788. https://doi.org/10.1002/2014gl060985

Fukushima, S., Shinohara, M., Nishida, K., Takeo, A., Yamada, T., & Yomogida, K. (2022). Detailed S-wave velocity structure of sediment and crust off Sanriku, Japan by a new analysis method for distributed acoustic sensing data using a seafloor cable and seismic interferometry. *Earth Planets and Space*, *74*(1), 92. https://doi.org/10.1186/s40623-022-01652-z

Gasperini, L., Stucchi, M., Cedro, V., Meghraoui, M., Ucarkus, G., & Polonia, A. (2021). Active fault segments along the North Anatolian fault system in the Sea of Marmara: Implication for seismic hazard. *Mediterranean Geoscience Reviews*, *3*(1), 29–44. https://doi.org/10.1007/s42990-021-00048-7

Hamilton, E. L. (1979). Sound velocity gradients in marine sediments. *Journal of the Acoustical Society of America*, *65*(4), 909–922. https://doi.org/10.1121/1.382594

Harris, R. A., Dolan, J. F., Hartleb, R. D., & Day, S. M. (2002). The 1999 Izmit, Turkey, earthquake: A 3D dynamic stress transfer model of intraearthquake triggering. *Bulletin of the Seismological Society of America*, *92*(1), 245–255. https://doi.org/10.1785/0120000825

Hartog, A. H. (2018). *An introduction to distributed optical fibre sensors*. Crc Press.

Herrmann, R. B. (2013). Computer programs in seismology: An evolving tool for instruction and research. *Seismological Research Letters*, *84*(6), 1081–1088. https://doi.org/10.1785/0220110096

Hubert-Ferrari, A., Barka, A., Jacques, E., Nalbant, S. S., Meyer, B., Armijo, R., et al. (2000). Seismic hazard in the Marmara Sea region following the 17 August 1999 Izmit earthquake. *Nature*, *404*(6775), 269–273. https://doi.org/10.1038/35005054

Kato, A., & Igarashi, T. (2012). Regional extent of the large coseismic slip zone of the 2011 Mw 9.0 Tohoku-Oki earthquake delineated by on-fault aftershocks. *Geophysical Research Letters*, *39*(15), L15301. https://doi.org/10.1029/2012gl052220

Kato, A., Miyatake, T., & Hirata, N. (2010). Asperity and barriers of the 2004 mid-Niigata prefecture earthquake revealed by highly dense seismic observations. *Bulletin of the Seismological Society of America*, *100*(1), 298–306. https://doi.org/10.1785/0120090218

Kirkpatrick, S. (1984). Optimization by simulated annealing: Quantitative studies. *Journal of Statistical Physics*, *34*(5–6), 975–986. https://doi.org/10.1007/bf01009452

Kurt, H., Sorlien, C. C., Seeber, L., Steckler, M. S., Shillington, D. J., Cifci, G., et al. (2013). Steady late quaternary slip rate on the Cinarcik section of the North Anatolian fault near Istanbul, Turkey. *Geophysical Research Letters*, *40*(17), 4555–4559. https://doi.org/10.1002/grl.50882

Lange, D., Kopp, H., Royer, J.-Y., Henry, P., Cakir, Z., Petersen, F., et al. (2019). Interseismic strain build-up on the submarine North Anatolian fault offshore Istanbul. *Nature Communications*, *10*(1), 3006. https://doi.org/10.1038/s41467-019-11016-z

Lindsey, N. J., Dawe, T. C., & Ajo-Franklin, J. B. (2019). Illuminating seafloor faults and ocean dynamics with dark fiber distributed acoustic sensing. *Science*, *366*(6469), 1103–1107. https://doi.org/10.1126/science.aay5881

Liu, Z., AlTheyab, A., Hanafy, S. M., & Schuster, G. (2017). Imaging near-surface heterogeneities by natural migration of backscattered surface waves: Field data test. *Geophysics*, *82*(3), S197–S205. https://doi.org/10.1190/geo2016-0253.1

Luu, K. (2021). disba: Numba-accelerated computation of surface wave dispersion (v0.6.1) [Software]. *Zenodo*. https://doi.org/10.5281/zenodo.5775195

Park, C. B., Miller, R. D., & Xia, J. (1998). Imaging dispersion curves of surface waves on multi-channel record. https://doi.org/10.1190/1.1820161

Polat, G., Nurcan, M. Ö., & Koulakov, I. (2016). Investigating P- and S-wave velocity structure beneath the Marmara region (Turkey) and the surrounding area from local earthquake tomography. *Earth Planets and Space*, *68*(1), 132. https://doi.org/10.1186/s40623-016-0503-4

Reilinger, R., McClusky, S., Vernant, P., Lawrence, S., Ergintav, S., Cakmak, R., et al. (2006). GPS constraints on continental deformation in the Africa-Arabia-Eurasia continental collision zone and implications for the dynamics of plate interactions. *Journal of Geophysical Research*, *111*(B5), B05411. https://doi.org/10.1029/2005jb004051

Sacchi, M. D., & Ulrych, T. J. (1995). High-resolution velocity gathers and offset space reconstruction. *Geophysics*, *60*(4), 1169–1177. https://doi.org/10.1190/1.1443845

Şengör, A. M. C., Tüysüz, O., İmren, C., Sakınç, M., Eyidoğan, H., Görür, N., et al. (2005). The North Anatolian fault: A new look. *Annual Review of Earth and Planetary Sciences*, *33*(1), 37–112. https://doi.org/10.1146/annurev.earth.32.101802.120415

Sladen, A., Rivet, D., Ampuero, J. P., De Barros, L., Hello, Y., Calbris, G., & Lamare, P. (2019). Distributed sensing of earthquakes and ocean-solid Earth interactions on seafloor telecom cables. *Nature Communications*, *10*(1), 5777. https://doi.org/10.1038/s41467-019-13793-z

Spica, Z. J., Castellanos, J. C., Viens, L., Nishida, K., Takeshi, A., Shinohara, M., & Yamada, T. (2022). Subsurface imaging with ocean-bottom distributed acoustic sensing and water phases reverberations. *Geophysical Research Letters*, *49*(2), e2021GL095287. https://doi.org/10.1029/2021gl095287

Spica, Z. J., Nishida, K., Akuhara, T., Pétrélis, F., Shinohara, M., & Yamada, T. (2020). Marine sediment characterized by ocean-bottom fiber-optic seismology. *Geophysical Research Letters*, *47*(16), e2020GL088360. https://doi.org/10.1029/2020gl088360

Wang, K., Luo, H., He, J., & Carvajal, M. (2024). Soft barrier to megathrust rupture enabled by serpentinized mantle wedge: The Chile subduction zone. *Earth and Planetary Science Letters*, *650*, 119115. https://doi.org/10.1016/j.epsl.2024.119115

Weaver, R. L. (2005). Information from seismic noise. *Science*, *307*(5715), 1568–1569. https://doi.org/10.1126/science.1109834

Williams, E. F., Fernández-Ruiz, M. R., Magalhaes, R., Roel, V., Zhan, Z., González-Herráez, M., & Martins, H. F. (2021). Scholte wave inversion and passive source imaging with ocean-bottom DAS. *The Leading Edge*, *40*(8), 576–583. https://doi.org/10.1190/tle40080576.1

Wright, T., Fielding, E., & Parsons, B. (2001). Triggered slip: Observations of the 17 August 1999 Izmit (Turkey) earthquake using radar interferometry. *Geophysical Research Letters*, *28*(6), 1079–1082. https://doi.org/10.1029/2000gl011776

Yılmaz, Z., Konca, A. Ö., & Ergintav, S. (2022). The effect of the 3-D structure on strain accumulation and the interseismic behavior along the North Anatolian fault in the Sea of Marmara. *Journal of Geophysical Research: Solid Earth*, *127*(3), e2021JB022838. https://doi.org/10.1029/2021jb022838

Zhan, Z. (2019). Distributed acoustic sensing turns fiber-optic cables into sensitive seismic antennas. *Seismological Research Letters*, *91*(1), 1–15. https://doi.org/10.1785/0220190112

Zhang, J. (2025a). Cross-correlation results of DAS data in the Marmara Sea (version 1) [Dataset]. *Zenodo*. https://doi.org/10.5281/zenodo.16741982

Zhang, J. (2025b). DAS data in Marmara Sea (version 1) [Dataset]. *Zenodo*. https://doi.org/10.5281/zenodo.15791919

Zhu, T., & Stensrud, D. J. (2019). Characterizing thunder-induced ground motions using fiber-optic distributed acoustic sensing array. *Journal of Geophysical Research: Atmospheres*, *124*(23), 12810–12823. https://doi.org/10.1029/2019jd031453